Planck early results IX : XMM-Newton follow-up for validation of Planck cluster candidates

Aghanim, N.

2011

Aghanim , N , Juvela , M , Keihänen , E , Keskitalo , R T , Kurki-Suonio , H , Poutanen , T J & Planck Collaboration 2011 , ' Planck early results IX : XMM-Newton follow-up for validation of Planck cluster candidates ' , Astronomy & Astrophysics , vol. 536 , pp. A9 . https://doi.org/10.1051/0004-6361/201

http://hdl.handle.net/10138/233725
https://doi.org/10.1051/0004-6361/201116460

other
publishedVersion

A&A 536, A9 (2011)
DOI: 10.1051/0004-6361/201116460

Astronomy & Astrophysics
Special feature

Planck early results

Planck early results. IX. *XMM-Newton* follow-up for validation of *Planck* cluster candidates⋆

Planck Collaboration: N. Aghanim[48], M. Arnaud[59], M. Ashdown[57,4], J. Aumont[48], C. Baccigalupi[70], A. Balbi[30], A. J. Banday[79,7,64], R. B. Barreiro[54], M. Bartelmann[78,64], J. G. Bartlett[3,55], E. Battaner[80], K. Benabed[49], A. Benoît[47], J.-P. Bernard[79,7], M. Bersanelli[27,42], R. Bhatia[5], J. J. Bock[55,8], A. Bonaldi[38], J. R. Bond[6], J. Borrill[63,74], F. R. Bouchet[49], M. L. Brown[4,57], M. Bucher[3], C. Burigana[41], P. Cabella[30], C. M. Cantalupo[63], J.-F. Cardoso[60,3,49], P. Carvalho[4], A. Catalano[3,58], L. Cayón[20], A. Challinor[51,57,11], A. Chamballu[45], L.-Y Chiang[50], G. Chon[65,4], P. R. Christensen[68,31], E. Churazov[64,73], D. L. Clements[45], S. Colafrancesco[39], S. Colombi[49], F. Couchot[62], A. Coulais[58], B. P. Crill[55,69], F. Cuttaia[41], A. Da Silva[10], H. Dahle[52,9], L. Danese[70], P. de Bernardis[26], G. de Gasperis[30], A. de Rosa[41], G. de Zotti[38,70], J. Delabrouille[3], J.-M. Delouis[49], F.-X. Désert[44], J. M. Diego[54], K. Dolag[64], S. Donzelli[42,52], O. Doré[55,8], U. Dörl[64], M. Douspis[48], X. Dupac[35], G. Efstathiou[51], T. A. Enßlin[64], F. Finelli[41], I. Flores-Cacho[53,32], O. Forni[79,7], M. Frailis[40], E. Franceschi[41], S. Fromenteau[3,48], S. Galeotta[40], K. Ganga[3,46], R. T. Génova-Santos[53,32], M. Giard[79,7], G. Giardino[36], Y. Giraud-Héraud[3], J. González-Nuevo[70], R. González-Riestra[34], K. M. Górski[55,82], S. Gratton[57,51], A. Gregorio[28], A. Gruppuso[41], D. Harrison[51,57], P. Heinämäki[77], S. Henrot-Versillé[62], C. Hernández-Monteagudo[64], D. Herranz[54], S. R. Hildebrandt[8,61,53], E. Hivon[49], M. Hobson[4], W. A. Holmes[55], W. Hovest[64], R. J. Hoyland[53], K. M. Huffenberger[81], G. Hurier[61], A. H. Jaffe[45], M. Juvela[19], E. Keihänen[19], R. Keskitalo[55,19], T. S. Kisner[63], R. Kneissl[33,5], L. Knox[22], H. Kurki-Suonio[19,37], G. Lagache[48], J.-M. Lamarre[58], A. Lasenby[4,57], R. J. Laureijs[36], C. R. Lawrence[55], M. Le Jeune[3], S. Leach[70], R. Leonardi[35,36,23], A. Liddle[18], M. Linden-Vørnle[13], M. López-Caniego[54], P. M. Lubin[23], J. F. Macías-Pérez[61], B. Maffei[56], D. Maino[27,42], N. Mandolesi[41], R. Mann[71], M. Maris[40], F. Marleau[15], E. Martínez-González[54], S. Masi[26], S. Matarrese[25], F. Matthai[64], P. Mazzotta[30], A. Melchiorri[26], J.-B. Melin[12], L. Mendes[35], A. Mennella[27,40], S. Mitra[55], M.-A. Miville-Deschênes[48,6], A. Moneti[49], L. Montier[79,7], G. Morgante[41], D. Mortlock[45], D. Munshi[72,51], A. Murphy[67], P. Naselsky[68,31], P. Natoli[29,2,41], C. B. Netterfield[15], H. U. Nørgaard-Nielsen[13], F. Noviello[48], D. Novikov[45], I. Novikov[68], S. Osborne[75], F. Pajot[48], F. Pasian[40], G. Patanchon[3], O. Perdereau[62], L. Perotto[61], F. Perrotta[70], F. Piacentini[26], M. Piat[3], E. Pierpaoli[17], R. Piffaretti[59,12], S. Plaszczynski[62], E. Pointecouteau[79,7], G. Polenta[2,39], N. Ponthieu[48], T. Poutanen[37,19,1], G. W. Pratt[59], G. Prézeau[8,55], S. Prunet[49], J.-L. Puget[48], R. Rebolo[53,32], M. Reinecke[64], C. Renault[61], S. Ricciardi[41], T. Riller[64], I. Ristorcelli[79,7], G. Rocha[55,8], C. Rosset[3], J. A. Rubiño-Martín[53,32], B. Rusholme[46], E. Saar[76], M. Sandri[41], D. Santos[61], B. M. Schaefer[78], D. Scott[16], M. D. Seiffert[55,8], G. F. Smoot[21,63,3], J.-L. Starck[59,12], F. Stivoli[43], V. Stolyarov[4], R. Sunyaev[64,73], J.-F. Sygnet[49], J. A. Tauber[36], L. Terenzi[41], L. Toffolatti[14], M. Tomasi[27,42], J.-P. Torre[48], M. Tristram[62], J. Tuovinen[66], L. Valenziano[41], L. Vibert[48], P. Vielva[54], F. Villa[41], N. Vittorio[30], B. D. Wandelt[49,24], S. D. M. White[64], D. Yvon[12], A. Zacchei[40], and A. Zonca[23]

(Affiliations can be found after the references)

Received 7 January 2011 / Accepted 2 July 2011

ABSTRACT

We present the *XMM-Newton* follow-up for confirmation of *Planck* cluster candidates. Twenty-five candidates have been observed to date using snapshot (∼10 ks) exposures, ten as part of a pilot programme to sample a low range of signal-to-noise ratios ($4 < S/N < 6$), and a further 15 in a programme to observe a sample of $S/N > 5$ candidates. The sensitivity and spatial resolution of *XMM-Newton* allows unambiguous discrimination between clusters and false candidates. The 4 false candidates have $S/N \leq 4.1$. A total of 21 candidates are confirmed as extended X-ray sources. Seventeen are single clusters, the majority of which are found to have highly irregular and disturbed morphologies (about ∼70%). The remaining four sources are multiple systems, including the unexpected discovery of a supercluster at $z = 0.45$. For 20 sources we are able to derive a redshift estimate from the X-ray Fe K line (albeit of variable quality). The new clusters span the redshift range $0.09 \lesssim z \lesssim 0.54$, with a median redshift of $z \sim 0.37$. A first determination is made of their X-ray properties including the characteristic size, which is used to improve the estimate of the SZ Compton parameter, Y_{500}. The follow-up validation programme has helped to optimise the *Planck* candidate selection process. It has also provided a preview of the X-ray properties of these newly-discovered clusters, allowing comparison with their SZ properties, and to the X-ray and SZ properties of known clusters observed in the *Planck* survey. Our results suggest that *Planck* may have started to reveal a non-negligible population of massive dynamically perturbed objects that is under-represented in X-ray surveys. However, despite their particular properties, these new clusters appear to follow the Y_{500}–Y_X relation established for X-ray selected objects, where Y_X is the product of the gas mass and temperature.

Key words. cosmology: observations – galaxies: clusters: general – galaxies: clusters: intracluster medium – cosmic background radiation – X-rays: galaxies: clusters

1. Introduction

The *Planck*[1] satellite has been surveying the sky across nine frequencies in the microwave band since August 2009. The resulting data set allows the detection of galaxy clusters through the Sunyaev-Zeldovich (SZ) effect (Sunyaev & Zeldovich 1972), the spectral distortion of the cosmic microwave background (CMB) generated via inverse Compton scattering of CMB photons by the hot electrons in the intra-cluster medium (ICM). The total SZ signal is expected to be closely related to the cluster

⋆ Corresponding author: E. Pointecouteau,
e-mail: etienne.pointecouteau@irap.omp.eu

[1] *Planck* (http://www.esa.int/Planck) is a project of the European Space Agency (ESA) with instruments provided by two scientific consortia funded by ESA member states (in particular the lead countries: France and Italy) with contributions from NASA (USA), and telescope reflectors provided in a collaboration between ESA and a scientific consortium led and funded by Denmark.

mass (e.g., da Silva et al. 2004) and its brightness is insensitive to redshift dimming. As a result, SZ surveys can potentially provide unbiased cluster samples, covering a wide range of redshifts, that are expected to be close to mass-selected. As compared to other SZ instruments, *Planck* brings a unique nine-band coverage from 30 to 857 GHz and a relatively high, band-dependent spatial resolution of 5–10 arcmin. Most crucially, the *Planck* SZ survey covers an exceptionally large volume, being the first all-sky survey capable of blindly detecting clusters since the ROSAT All-Sky Survey (RASS) in the X-ray domain. As a consequence, *Planck* is detecting previously unknown, massive clusters that do not appear in other SZ surveys. Its all-sky coverage allows detection of the rarest clusters, the most massive objects lying in the exponential tail of the mass function. These are the best clusters for precision cosmology: their abundance evolution is the most sensitive to the cosmological parameters (Voit 2005), and their gas mass fractions can be used as distance indicators (Allen et al. 2008). In addition, clusters in this high-mass regime are X-ray bright, making their observation easier, and their ICM is expected to be the least affected by non-gravitational processes. These newly-discovered *Planck* clusters will thus also be ideal targets for studying the physics of the gravitational collapse that drives all cluster formation.

The *Planck* survey is providing a sample of cluster *candidates*. Any such survey sample is expected to include a fraction of false detections, due for example to fluctuations in the complex microwave astrophysical sky. In addition, as a result of *Planck*'s moderate spatial resolution at SZ frequencies with respect to typical cluster sizes, a *Planck* cluster candidate SZ measurement essentially provides only coordinates and total SZ flux estimates; these estimates are further hampered by the flux-size degeneracy discussed extensively in Planck Collaboration (2011d). A vigourous follow-up programme is therefore required to scientifically exploit *Planck* cluster candidate data. Such a programme includes candidate confirmation, which is the final part of the catalogue validation, in addition to redshift measurements, estimation of relevant physical parameters (including cluster size, allowing precise SZ flux estimates), and investigation of scaling properties. In particular, measurement of the relation between the SZ "luminosity" and the mass as a function of redshift, z, is essential for calculation of the survey selection function and for related cosmological applications.

The all-sky nature of the *Planck* survey means that confirmation and redshift measurement of cluster candidates is not a trivial task. In the optical domain, the only publicly available large survey is the Sloan Digital Sky Survey (SDSS)[2]. Although cross-correlation with this survey can be used to confirm candidates up to $z \sim 0.6$, it covers only part of the northern sky. Furthermore, optical confirmation is hampered by the relatively large *Planck* source position uncertainty, which can be up to 5′ (Planck Collaboration 2011d). To discriminate between a true counterpart and a chance association with low-mass systems at various redshifts within the *Planck* error box, optical mass and spectroscopic redshift or photometric redshift estimates with a wide-field, multi-band, instrument are required.

In contrast, confirmation in X-rays offers definite advantages. Above the Galactic Plane, the detection of extended X-ray emission is an unambiguous signature of a cluster, and the density-squared dependence of the X-ray emission reduces projection effects nearly to zero. Furthermore, the low space density of groups and clusters in a typical X-ray exposure makes spurious association with a *Planck* candidate unlikely. For instance, the XMM-LSS survey found 29 systems in 5 deg^2 using 10 ks *XMM-Newton* exposures (Pacaud et al. 2007). Such a detection rate corresponds to only a 10 per cent probability of finding a cluster by chance within a 5′ aperture, the conservative *Planck* error box. Finally, as both X-ray and SZ observations probe the same medium, spurious associations can be readily assessed from a consistency check between the X-ray and SZ flux, assuming a reasonable redshift range (as illustrated in Sect. 3.2).

In this context, and because of its superior sensitivity, *XMM-Newton* (Jansen et al. 2001) is the best instrument for following up newly-detected *Planck* clusters up to high redshift. A short snapshot *XMM-Newton* exposure is sufficient to confirm any *Planck* cluster candidate at least up to $z = 1.5$ (Sect. 2.4), and for the X-ray brightest objects, provides the source redshift from the iron K line (Sect. 4.1). Because of their high mass, clusters are expected to be larger than 1′ and the *XMM-Newton* spatial resolution is sufficient to discriminate between a point source and extended emission.

In order to assess the galaxy cluster nature of the *Planck* SZ sources and to help guarantee the integrity of the final *Planck* SZ legacy catalogue to be released in 2012, we have thus proposed to use *XMM-Newton* to confirm the highest significance cluster candidates discovered by *Planck*. This validation programme consists of snapshot (∼10 ks) observations and is undertaken via an agreement between the ESA *XMM-Newton* and *Planck* project scientists. In this paper we present the definition and results of this programme. To date, 25 *Planck* SZ sources have been observed, making use of *XMM-Newton* Director's Discretionary Time. Of these, 21 sources have been confirmed. In compliance with *Planck* policies for follow-up, the *XMM-Newton* data of the 25 *Planck* sources are made public along with the publication of the Early Release Compact Source Catalogue (ERCSC).

The *XMM-Newton* follow-up for validation is the backbone of a larger programme for the confirmation and redshift measurement of *Planck* SZ cluster candidates. The *Planck* collaboration has also been granted time on the following facilities: the ENO, the ESO/MPG 2.2 m and the Palomar telescopes. Observations with these facilities are ongoing or being processed. Some optical results from the ENO observations are presented together with the *XMM-Newton* results in this paper (Sects. 4.2 and A.1). Other early astrophysics results on clusters of galaxies are presented in Planck Collaboration (2011d,f,g,h).

We adopt a ΛCDM cosmology with $H_0 = 70\ \mathrm{km\,s^{-1}\,Mpc^{-1}}$, $\Omega_\mathrm{M} = 0.3$ and $\Omega_\Lambda = 0.7$. The factor $E(z) = \sqrt{\Omega_\mathrm{M}(1+z)^3 + \Omega_\Lambda}$ is the ratio of the Hubble constant at redshift z to its present day value. The quantities M_{500} and R_{500} are the total mass and radius corresponding to a total density contrast $\delta = 500$, as compared to $\rho_\mathrm{c}(z)$, the critical density of the Universe at the cluster redshift; thus $M_{500} = (4\pi/3)\,500\,\rho_c(z)\,R_{500}^3$. The quantity Y_X is defined as the product of $M_{\mathrm{g},500}$, the gas mass within R_{500}, and T_X, the spectroscopic temperature measured in the [0.15–0.75] R_{500} aperture. The SZ signal is characterised by Y_{500} throughout. This quantity is defined as $Y_{500}D_\mathrm{A}^2 = (\sigma_\mathrm{T}/m_\mathrm{e}c^2)\int P\mathrm{d}V$. Here D_A is the angular-diameter distance to the system, σ_T is the Thomson cross-section, c is the speed of light, m_e is the electron rest mass; $P = n_\mathrm{e}T$ is the pressure, the product of the electron number density and temperature, and the integration is performed over a sphere of radius R_{500}. The quantity $Y_{500}\,D_\mathrm{A}^2$ is the spherically integrated Compton parameter and Y_{500} is proportional to the apparent magnitude of the SZ signal from within R_{500}.

[2] http://www.sdss.org/

2. The *XMM-Newton* validation follow-up of *Planck* cluster candidates

2.1. The Planck survey

Planck (Tauber et al. 2010; Planck Collaboration 2011a) is the third generation space mission to measure the anisotropy of the CMB. It observes the sky in nine frequency bands covering 30–857 GHz with high sensitivity and angular resolution from 31′ to 5′. The Low Frequency Instrument (LFI; Mandolesi et al. 2010; Bersanelli et al. 2010; Mennella et al. 2011 covers the 30, 44, and 70 GHz bands with amplifiers cooled to 20 K. The High Frequency Instrument (HFI; Lamarre et al. 2010; Planck HFI Core Team 2011a) covers the 100, 143, 217, 353, 545, and 857 GHz bands with bolometers cooled to 0.1 K. Polarisation is measured in all but the highest two bands (Leahy et al. 2010; Rosset et al. 2010). A combination of radiative cooling and three mechanical coolers produces the temperatures needed for the detectors and optics (Planck Collaboration 2011b). Two data processing centres (DPCs) check and calibrate the data and make maps of the sky (Planck HFI Core Team 2011b; Zacchei et al. 2011). *Planck*'s sensitivity, angular resolution, and frequency coverage make it a powerful instrument for Galactic and extragalactic astrophysics as well as cosmology. Early astrophysics results are given in Planck Collaboration (2011h–z).

2.2. Blind detection of SZ clusters in Planck

The blind search for clusters in *Planck* data relies on a multi-matched filter (MMF) approach (Melin et al. 2006)[3]. This detection algorithm operates on all-sky maps divided into a set of overlapping square patches, using simultaneously the 6 frequency maps of the HFI instrument (Planck Collaboration 2011d). Within the algorithm, the SZ spectral signature and the universal pressure profile derived by Arnaud et al. (2010) are used as spectral and spatial templates, respectively. In such a blind search, the position, the characteristic scale of the profile ($\propto R_{500}$) and the amplitude ($\propto Y_{500}$) are left free, being optimised by the MMF algorithm. In practice the algorithm is run in an iterative way: after a first detection run to locate candidates, consecutive runs on sky patches centred on the candidate positions refine the estimated signal-to-noise ratio (S/N) and other properties.

Cluster candidates then undergo a validation process, extensively described in Planck Collaboration (2011d). This process includes internal quality checks (e.g., map artefacts, cross-comparison between detection algorithms, SZ spectral signature, astrophysical contamination by Galactic dust, point sources or structures in the CMB) and cross-correlation with ancillary data and catalogues allowing known clusters to be identified. This process produces a list of new *Planck* SZ cluster candidates above a given S/N threshold (S/N = 4 in this work).

2.3. XMM-Newton target selection

From the list of new potential clusters detected as SZ sources in the *Planck* survey, we selected 25 targets in a two step process:

1. Pilot programme: 10 targets were selected on the basis of the *Planck* survey as it stood at the end of October 2009, i.e., ~62% sky coverage. These targets were explicitly chosen to sample the lower range of signal-to-noise ($4 < S/N < 6$) in order to better characterise the nature and quality of the SZ signal.
2. High S/N programme: a further 15 targets were chosen in the spring of 2010 when the first full-sky coverage was close to completion (99.5% sky coverage). In contrast to the pilot programme, here we focused on high-significance SZ sources ($S/N > 5$) and selected candidates starting from the highest S/N.

In both cases the selection process was intimately linked to the *Planck*-HFI data time ordered information processing status, calibration, attitude and map versions (as of Dec. 7, 2009 and April 19, 2010 for the two programmes, respectively). The choice of targets was also constrained by their *XMM-Newton* visibility in a period of 2–3 months following their submission to the science operations centre. For both programmes, maps and spectra of each potential target were visually inspected, including reprocessing with aperture photometry methods. Cross-correlation with the RASS Bright Source Catalogue (RASS-BSC, Voges et al. 1999) and Faint Source Catalogue (RASS-FSC, Voges et al. 2000) was undertaken. For the two targets of the pilot programme falling in the SDSS area, we ran a dedicated algorithm to search for galaxy overdensities (Fromenteau et al., in prep.), allowing us to track significant concentrations of matter down to $z \sim 0.6$. These two targets were chosen to test the SDSS based confirmation at high z. The first candidate, PLCK G070.8-21.5, was not confirmed (see Fromenteau et al., in prep., for discussion); the other candidate, PLCK G214.6+37.0, is discussed in Sect. 7.2.1. Detailed searches in *XMM-Newton*, *Chandra* and *Suzaku* observatory logs were also undertaken in order to avoid duplication of performed or accepted observations with similar facilities.

Six of the ten pilot programme targets were confirmed (see Table 1); two of these are multiple systems. Taking into account the result of the pilot project, for the second programme we set a lower S/N threshold of S/N = 5 and refined and strengthened the selection criteria. In particular, we required that the source be independently detected by at least two of the three blind detection methods, and more quality flags were considered. The internal checks were very similar to those defined for constructing the early SZ (ESZ) sample (Planck Collaboration 2011d), which benefit from the result of the *XMM-Newton* Pilot programme. We also performed a search for emission in the RASS hard band images, looking for X-ray signatures beyond those recorded in the RASS source catalogues. However, RASS information never took precedence over the internal *Planck* quality flags. Note that two of the false candidates of the Pilot programme (PLCK G343.4–43.4 and PLCK G226.1–16.9) were associated with a RASS-FSC source that *XMM-Newton* subsequently revealed to be several point sources (see Sect. 3.2). Thus association with an RASS source alone is not sufficient for cluster candidate confirmation.

The ESZ sample (Planck Collaboration 2011d) consists of a high signal-to-noise, i.e. primarily $S/N \geq 6$, list of 189 clusters and cluster candidates based on data from the first 10 months of the *Planck* survey. Ten of the 21 objects presented in the present paper passed the S/N ESZ selection criteria and are thus part of the ESZ sample released to the community in January 2011. The original S/N of their detection in the *Planck* maps is given in Table 1, whereas the S/N values provided in Table 2 are derived from the 10 month *Planck* maps on the basis of which the ESZ sample was constructed.

[3] Results from other methods have been cross-compared to those from the MMF search, including from the PowellSnakes-based algorithm (Carvalho et al. 2009).

Table 1. Observation log of the *XMM-Newton* validation follow-up.

Name	S/N	RA_{SZ} (deg)	Dec_{SZ} (deg)	OBSID	Filter	t_{exp} (ks EPN)	Clean fraction (MOS/EPN)	Confirmed
PLCK G277.8−51.7	6.1	43.596	−58.964	0656200301	THIN	16.5	0.5/0.2	Y ESZ
PLCK G334.8−38.0*	4.9	313.177	−61.202	0656200701	THIN	21.2	0.8/0.5	Y
PLCK G250.0+24.1	4.9	143.042	−17.647	0656200401	THIN	10.4	0/0	Y
PLCK G286.3−38.4	4.7	59.800	−72.067	0656200501	THIN	13.6	0.7/0	Y
PLCK G004.5−19.5	4.6	289.226	−33.509	0656201001	MED	10.0	1/0.6	Y
PLCK G214.6+36.9*	4.2	137.206	14.642	0656200101	THIN	17.6	0.7/0.7	Y
PLCK G070.8−21.5	4.1	321.410	19.941	0656200201	MED	25.4	0.4/0.1	...
PLCK G317.4−54.1	4.1	355.247	−61.038	0656200801	THIN	12.0	0.9/0.7	...
PLCK G226.1−16.9	4.0	93.139	−19.040	0656200601	THIN	10.0	0.7/0.4	...
PLCK G343.4−43.4	3.9	320.145	−53.631	0656200901	MED	10.0	0.9/0.9	...
PLCK G287.0+32.9	10.2	177.714	−28.074	0656201201	THIN	10.0	0.7/0.4	Y ESZ
PLCK G171.9−40.7	10.7	48.231	8.380	0656201101	THIN	10.0	1/0.8	Y ESZ
PLCK G285.0−23.7	8.3	110.805	−73.457	0656201401	THIN	10.0	0.9/0.6	Y ESZ
PLCK G271.2−31.0	8.3	87.315	−62.087	0656201301	THIN	10.0	1/1	Y ESZ
PLCK G262.7−40.9	7.4	69.624	−54.309	0656201601	THIN	14.7	1/0.9	Y ESZ
PLCK G308.3−20.2*	7.4	229.588	−81.523	0656201501	THIN	10.0	1/1	Y ESZ
PLCK G337.1−26.0*	6.4	288.583	−59.513	0656201701	THIN	13.7	1/1	Y ESZ
PLCK G292.5+22.0	6.2	180.241	−39.889	0656201801	MED	13.2	0.6/0.5	Y ESZ
PLCK G205.0−63.0	6.1	41.593	−20.527	0656201901	THIN	11.7	1/1	Y
PLCK G241.2−28.7	5.9	85.768	−36.022	0656202001	THIN	10.0	1/1	Y
PLCK G286.6−31.3	5.9	82.8430	−75.164	0656202101	THIN	10.0	0.7/0.3	Y ESZ
PLCK G018.7+23.6	5.6	255.553	−1.004	0656202201	THIN	7.2	1/1	Y
PLCK G100.2−30.4	5.5	350.589	28.563	0656202301	THIN	10.0	0.9/0.7	Y
PLCK G272.9+48.8	5.1	173.310	−9.479	0656202601	THIN	11.7	0/0	Y
PLCK G285.6−17.2	5.2	130.956	−71.190	0656202501	THIN	10.0	1/1	Y ESZ

Notes. The 10 targets of the pilot programme are listed first. Column (1): *Planck* source name. Asterisked objects denote sources that were found to be multiple systems in X-rays. Column (2): signal-to-noise ratio of the detection of the *Planck* cluster candidate in the version of the *Planck*-HFI maps available for each programme. Columns (3) and (4): right ascension and declination of the *Planck* source (J2000). Columns (5)–(8): *XMM-Newton* observation identification number, filter used, on-source exposure time with the EPN camera and fraction of useful time after cleaning for periods of high background due to soft proton flares (EMOS and EPN camera, see also Sect. 2.5). Column (9): confirmed clusters are flagged. Those included in the ESZ sample (Planck Collaboration 2011d) are also identified.

2.4. Observation setup

As discussed by Scharf (2002), the optimum energy band for *XMM-Newton* cluster detection is the soft energy band (energy below 2 keV), for which the signal-to-noise ratio reaches a maximum. We calculated expectations for *XMM-Newton* sensitivity in that band for two representative values of the SZ flux from within R_{500}: $Y_{500} = 5 \times 10^{-4}$ arcmin^{-2} and $Y_{500} = 2 \times 10^{-3}$ arcmin^{-2}. In each case, the expected cluster luminosity L_{500} for various redshifts was estimated using the L_{500}–$D_A^2 Y_{500}$ relation of Arnaud et al. (2010), assuming self-similar evolution. We then derived the corresponding total *XMM-Newton* count rates, R, in the [0.3−2] keV band for the EPIC MOS–CCD (herafter EMOS) and pn–CCD (herafter EPN) camera (Turner et al. 2001; Strüder et al. 2001). We used the `xspec` software (Arnaud 1996) to simulate an absorbed thermal model (assuming $kT = 7$ keV, $N_H = 2 \times 10^{20}$ cm^{-2}), convolved with the instrument response. The corresponding angular extent θ_{500} was estimated from the L_{500}–M_{500} relation of Pratt et al. (2009). The signal–to–noise ratio of the detection is then given by $S/N = (R\sqrt{t_{exp}})/(\sqrt{R + (2 R_{bkg} A)})$, where t_{exp} is the exposure time, R_{bkg} is the background count rate, and $A = 4\pi\theta_{500}^2$ is the integration area in square arc minutes. We assumed a [0.3–2] keV band background count rate of $R_{bkg} = 4.5 \times 10^{-3}$ counts s^{-1} arcmin^{-2}, as estimated from the blank sky backgrounds of Read & Ponman (2003). Figure 1 shows the resulting S/N of an *XMM-Newton* detection as a function of redshift.

Since the goal of the *XMM-Newton* observations is confirmation of new *Planck* SZ cluster candidates, the nominal observing time was set to 10 ks (net EPN camera time) per target. Such a snapshot observation is sufficient to detect the cluster – if real – at better than 10σ up to $z = 1.5$ (Fig. 1). The nominal setup used the THIN filters (unless optical loading had to be avoided) and EFF mode for the EPN camera. The boresight was optimised to avoid camera gaps.

2.5. XMM-Newton data reduction

We produced calibrated event lists using v10.0 of the *XMM-Newton* science analysis system (SAS). Observations were cleaned for periods of high background due to soft proton flares, PATTERN-selected and corrected for vignetting as described in Pratt et al. (2007). Point sources were identified from the small scales of wavelet-decomposed images in the [0.3–2] and [2−5] keV bands. These sources were excluded in the analysis of confirmed clusters, with the exclusion radius matched to the point spread function (PSF) size (which varies across the detector).

Above ∼2 keV the *XMM-Newton* background is dominated by particle events. We subtracted this background using a

stacked event list built from observations obtained with the filter wheel in the CLOSED position, recast to the pointing position and renormalised using the count rate in the high energy band free of cluster emission. The remaining background (due to the cosmic X-ray background of unresolved AGN and Galactic emission) was estimated from the particle-background subtracted emission from an annulus beyond the cluster emission. For the spectral analysis, we modeled this background emission as arising from two thermal sources and a power-law source with index $\Gamma = 1.4$, taking into account the absorbing Galactic column density in the direction of the object (see, e.g., De Luca & Molendi 2004).

As Table 1 shows, the observations are of variable quality. In three cases the EPN data were completely contaminated by soft proton flares and formally had no useful observing time. For two of these observations, the EMOS data were completely contaminated too. In these instances, we used EMOS data only (uncleaned in the last two cases). The power-law index in the background model was left free, which empirically produces a relatively good fit to the background spectrum. The spectroscopic results for these objects should be treated with caution.

Spectral fits were undertaken in the [0.3–10] keV energy range, after binning the spectra to a minimum of 25 counts per bin and excluding background fluorescence line regions. The cluster component was modelled with an absorbed MEKAL model with the reference solar abundances from the data of Anders & Grevesse (1989). The hydrogen column density $N_{\rm H}$ was fixed at the 21 cm value from Dickey & Lockman (1990), except for PLCK G286.3−38.4, PLCK G308.3−20.2 and PLCK G018.7+23.6. Their best fit $N_{\rm H}$ values were found to be significantly higher by a factor 1.8, 1.8 and 2.4, respectively. These clusters are located at low latitude, in regions of high IR dust emission (Snowden et al. 1997, Fig. 11). The 21 cm value may underestimate the total $N_{\rm H}$, measured from X-ray data, due to a non-negligible H_2 contribution. To check this hypothesis, we used the IRIS maps (Miville-Deschênes & Lagache 2005) as tracers of the dust emission and the correlation between the Galactic dust emission and the total hydrogen column density (Boulanger et al. 1996) to estimate the $N_{\rm H}$ values at the cluster locations (see Pointecouteau et al. 2004). A better agreement was found with X-ray values, with ratios of 1.30, 1.06 and 1.48. It must also be noted that the PLCK G286.3−38.4 observation is highly contaminated by solar flares and only EMOS data are used. Some residual background may also affect the low energy part of the spectrum and thus the $N_{\rm H}$ estimate

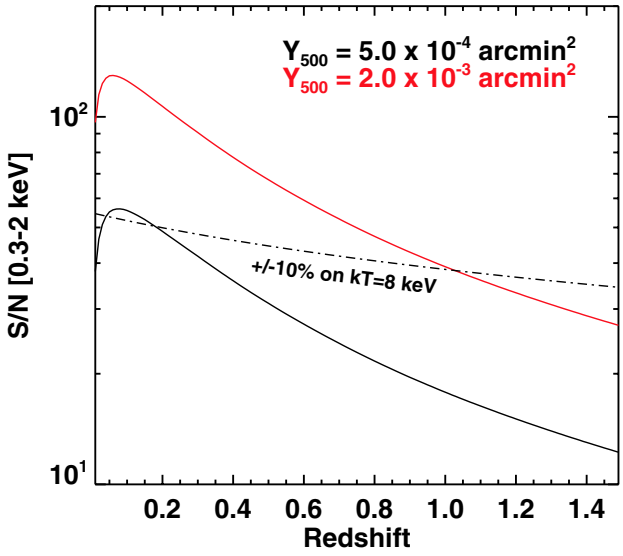

Fig. 1. Sensitivity of *XMM-Newton* observations to typical *Planck* SZ sources. The expected signal-to-noise ratio (S/N) of the cluster detection in the [0.3–2] keV energy band with the EPIC camera is plotted as a function of redshift for an exposure time of 10 ks assuming two typical SZ fluxes. See text for details of the model assumed to convert SZ to X-ray flux and count rate. The dash-dotted line indicates the S/N required for 10% uncertainty on the temperature measurement of an 8 keV cluster.

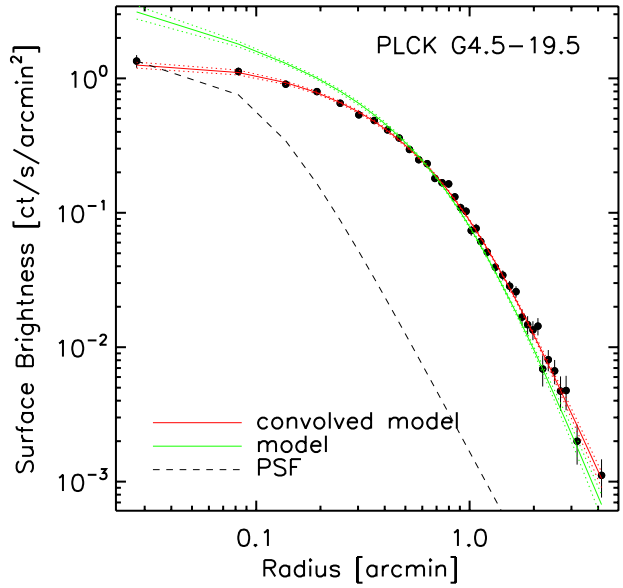

Fig. 2. Surface brightness profile of PLCK G4.5-19.5 at $z = 0.54$, the highest-z cluster of the sample, as measured with *XMM-Newton*. The data of the EMOS1&2 and EPN camera in the [0.3–2.] keV energy band are combined. The green line indicates the best fitting model (see text); the red line is the best fitting model convolved with the point spread function (PSF) of *XMM-Newton* and the dashed line is the on axis XMM/PSF, normalised to the central intensity. The source is clearly extended.

3. *XMM-Newton* validation: methods and outcome

The observations were completed by the end of October 2010. The median clean EPN observation time is 7 ks (Table 1). Of 25 targets, 21 are confirmed as X-ray extended sources. Only four targets with S/N ≤ 4.1 were not confirmed. The confirmation status of each *XMM-Newton* observation is given in Table 1.

3.1. Confirmed cluster candidates

Our procedure for candidate cluster confirmation consists of identifying an extended X-ray source coincident with the *Planck* SZ source and checking that the SZ and X-ray properties are consistent. Generally, a candidate cluster (or supercluster) is clearly visible within 5′ of the *Planck* candidate position, in which case we simply have to confirm the X-ray source extent. This is achieved by comparing the surface brightness profile extracted in the [0.3–2.0] keV band with the *XMM-Newton* PSF. A typical cluster β-model with a cusp (Eq. (2) in Pratt & Arnaud 2002) is also fitted to the data. Figure 2 shows this comparison for the highest-z confirmed extended source.

17 systems show extended emission from a single source and are confirmed as new clusters of galaxies. Using the Fe K line in the X-ray spectrum we have estimated a redshift for all these objects, albeit with large uncertainties in some cases (see Sect. 4.1). We have also calculated the $Y_{\rm X}$ parameter (Sect. 5.1). A final check of the candidate confirmation is the good agree-

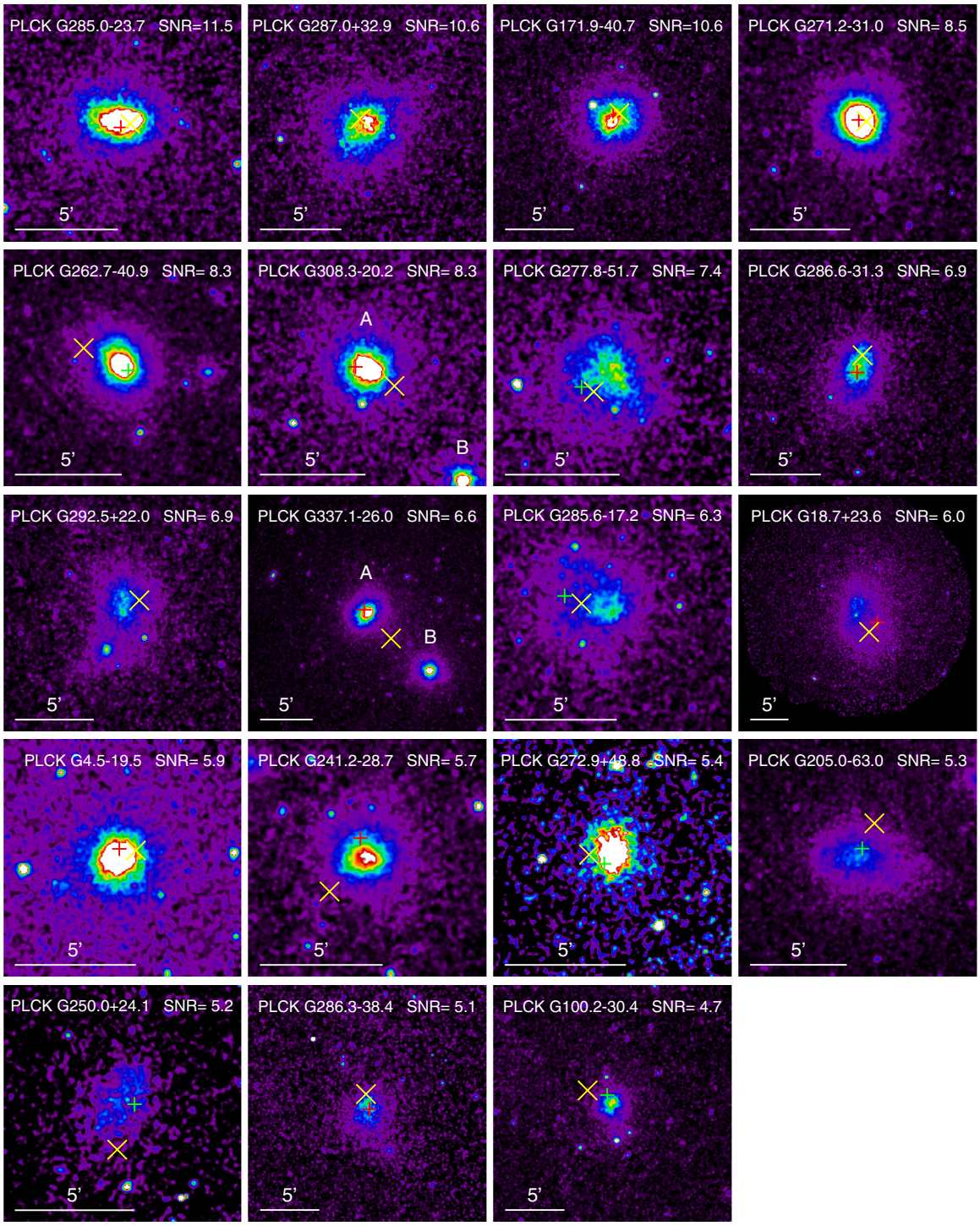

Fig. 3. *XMM-Newton* images of all confirmed cluster candidates, except for the two triple systems which are shown on Fig. 12 and discussed in Sect. 7, in the [0.3–2] keV energy band. The observations of PLCK G272.9+48.8 and PLCK G250.0+24.1 suffer from high background that has only been crudely subtracted. Image sizes are $3\theta_{500}$ on a side, where θ_{500} is estimated from the M_{500}–Y_X relation (see Sect. 5.1). Images are corrected for surface brightness dimming with z, divided by the emissivity in the energy band, taking into account galactic absorption and instrument response, and scaled according to the self-similar model. The colour table is the same for all clusters, so that the images would be identical if clusters obeyed strict self-similarity. The majority of the objects show evidence for significant morphological disturbance. A yellow cross indicates the *Planck* position and a red/green plus sign the position of a RASS-BSC/FSC source.

ment found between the measured SZ signal and that expected from the Y_X value (Sect. 5.1). A further two confirmed candidates were revealed to be double systems, one of which is a projection of two independent clusters at different redshifts. More unexpected are two additional newly-discovered triple systems. All of the confirmed candidates revealed by *XMM-Newton* to be multiple clusters are discussed in more detail in Sect. 7.

The *XMM-Newton* images of confirmed single and double systems are shown in Fig. 3. In each panel, the *Planck* source centre position is marked with a cross; in addition, when rele-

vant a red/green plus sign shows the associated RASS-FSC/BSC source.

3.2. False cluster candidates

In some cases a source is not clearly visible in the image and then the relatively large FWHMs of the HFI beams (~4′.5–9′.5; Planck HFI Core Team 2011b) complicate source search and confirmation. For these observations we employ the approach described in Šuhada et al. (2010), applying the *XMM-Newton*–SAS source detection algorithms `eboxdetect` and `emldetect` to the images to determine whether an extended source lies within the *Planck* beam. In brief, images are produced in the [0.35–2.4] keV band and `eboxdetect` is first run in local mode, where the background is estimated locally for each source. Sources found in this first step are then excised, leaving an image suitable for background estimation. The background image is modeled with two components, a vignetted component to represent the X-ray background, and a non-vignetted component to represent the particle and instrumental background. The model is based on a linear combination of two templates based on vignetted and non-vignetted exposure maps, and is fit to the source-subtracted image. We then re-run `eboxdetect` with this model background. All sources found in this step are then analysed with the maximum likelihood (ML) task `emldetect`, that analyses each source by fitting with a 2D King function convolved with the PSF. The log of the detection likelihood of each source as defined in the code is `det_ml` $= -\ln P_{\rm rand}$, where the latter is the probability of the observed counts arising from Poisson fluctuations. We set the minimum `det_ml` = 6, corresponding to a $\gtrsim 3\sigma$ detection[4]. In addition to the above, we also searched for possible extended sources using visual inspection of a wavelet-smoothed image.

Figure 4 illustrates application of the method for the false source PLCK G226.1−16.9. This candidate was the lowest S/N candidate of the Pilot sample (S/N = 4.0) and located close to a RASS-FSC source, which may have been the cluster counterpart. The top panel shows the raw *XMM-Newton* image and the reconstructed EPN ML source image. The RASS-FSC source located at 0.8′ from the *Planck* source is clearly detected with *XMM-Newton* (red plus sign in the top panels). The surface brightness profile is well fitted by a point source convolved with the *XMM-Newton* PSF (bottom left panel). The source spectrum is clearly a power law, and thermal emission from a 0.3 solar abundance ICM is rejected at high confidence at all redshifts and temperatures. This source is most likely an AGN and is definitively not the *Planck* counterpart.

The source list produced by the ML method includes two potentially extended sources, only one of which is within 5′ of the *Planck* source position (source labelled A in the figure). It is located ~0.8′ from the RASS-FSC source position and is much fainter, showing the capability of *XMM-Newton* to separate sources. The source has an estimated [0.35–2.4] keV flux of $\sim 2 \times 10^{-14}$ erg cm^2 s^{-1}, which is more than 5 times lower than that expected from the SZ source even if located at $z \sim 1.5$. Furthermore its extent (although not well constrained) is small and it is perfectly coincident with a 2MASS galaxy. This source again could not be the *Planck* counterpart. Finally, from a wavelet-smoothed image, there was a hint that another source, located 3.5′ away from the *Planck* candidate position, was extended, although it was not classified as such with the ML method (source labelled B). We extracted its profile and confirmed it as extended, although the extent was not very significant (bottom right panel of Fig. 4). However, its flux was half that expected from the observed *Planck* flux, even for a cluster at $z = 1.5$. Nevertheless, in view of possible errors in the *Planck* position, we re-analysed the *Planck* data by re-extracting the signal exactly at the position of the source. The SZ detection was no longer significant, leading us to conclude that source B was definitively not the counterpart to the *Planck* candidate. From the *XMM-Newton* observation we thus concluded that this *Planck* candidate was a false detection.

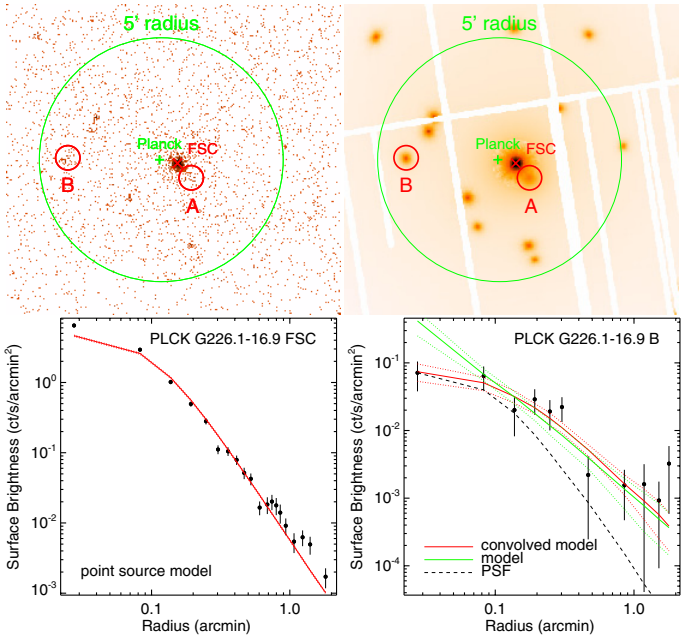

Fig. 4. Illustration of the *XMM-Newton* validation procedure results for a false candidate, PLCK G226.1−16.9. *Top panels*: sum of the EMOS and EPN raw image (*left*) and reconstructed EPN image (*right*) in the soft band. The circle of 5′ radius centred on the *Planck* position (green cross) corresponds to the conservative position error box. The RASS-FSC source is clearly detected (red cross) as a point source: its surface brightness profile (black points in *left bottom panel*) is well fitted by the *XMM-Newton* PSF (red line). Two extended sources labelled A and B are also detected. *Bottom right panel*: same as Fig. 2 for source B.

4. Redshift estimate

4.1. XMM-Newton estimates

The ICM has a typical abundance of 0.3 times solar, implying that metals are present in large amounts (see Balestra et al. 2007; Leccardi & Molendi 2008; Maughan et al. 2008, for recent work on metals in the cluster context). The spectroscopic sensitivity of *XMM-Newton* allows the measurement of the intensity and centroid energy of the strongest line emission, namely the Fe K and Fe L line complexes (respectively found at $E \sim 6.4$ and $E \sim 1$ keV at $z = 0$). As a consequence the Fe line emission can be used to constrain the cluster redshift. We have thus searched for their signature in the *XMM-Newton* observations, focusing mainly on the Fe K complex, which is about 10 times as strong as any other line emission in the ICM. A clear detection then provides an estimate of the X-ray redshift $z_{\rm Fe}$.

The intrinsic spectral resolution of *XMM-Newton* is $\Delta E \sim 150$ eV at 6.4 keV and $\Delta E \sim 100$ eV at 3.2 keV; the ener-

[4] See http://xmm.esac.esa.int/sas/current/doc/emldetect/node3.html for more details

gies here correspond to the Fe K complex centroid energy for a cluster at a redshift of $z = 0$ and $z = 1$, respectively. Such resolution allows centroid determination to typically 10–15 eV for high quality spectra, of the same magnitude as the systematic uncertainty of the calibration of the energy reconstruction (about 5 eV and 10 eV in the central CCD of the EMOS and EPN camera, respectively). The overall energy uncertainty would yield a typical corresponding redshift uncertainty of $\Delta z \sim 0.002$. In practice, the limiting factor affecting the accuracy of the redshift determination is the statistical uncertainty in the spectrum, which is linked to the observation duration and overall quality (background conditions). Furthermore, *Planck*-detected clusters are mostly massive, hot objects with low Fe K line equivalent widths (Rothenflug & Arnaud 1985). This makes $z_{\rm Fe}$ determination more difficult than for cooler objects.

To estimate $z_{\rm Fe}$ using `xspec` we first performed a spectral fit of the region corresponding to the maximum significance of the detection (defined from the surface brightness profile in the soft band), with the redshift as one of the free parameters. The abundance was left free to fit within a typical cluster range (0.2–0.6 times solar). From this starting point we investigated the χ^2 in the kT–$z_{\rm Fe}$ plane using a regular grid. The best fitting kT and $z_{\rm Fe}$ values were recovered from a simple maximum likelihood analysis, whereupon these best fitting values were used as input for a final spectral fit. When a two- or three-peak degeneracy appeared in the kT–$z_{\rm Fe}$ plane, we checked the various potential $z_{\rm Fe}$ values and chose the redshift giving the best spectral fit as defined by the χ^2 and the null probability hypothesis.

This redshift estimation process is illustrated by three cases in Fig. 5 with the left panel showing a fully degenerate case, the middle panel a double-peaked case and the right panel a well-constrained case. These redshifts are flagged with quality values $Q_z = 0, 1, 2$, respectively, in Table 2. The few cases where no redshift estimate was possible are flagged with $Q_z = -1$.

4.2. Optical estimates

For three clusters, we have estimated the redshift either from existing optical archive observations or dedicated follow-up observations as part of the overall *Planck* cluster candidate validation programme. The most recent corresponds to telescope time acquired by the *Planck* consortium at the ENO telescopes, Observatorio del Teide (Tenerife, Spain – AO 2010A and 2010B). The details of the observation setup and data processing can be found in Appendix A.1.

- PLCK G100.2−30.4. The source was observed in 4 bands (*griz*) with the CAMELOT camera at the 0.82-m IAC80 telescope. After data reduction, we derived a photometric redshift of $z_{\rm phot} = 0.38 \pm 0.04$, using the BPZ code (Benítez 2000). This estimate is compatible within 3σ, with the $z_{\rm Fe} = 0.31$ derived from the X-ray spectroscopy.
- PLCK G285.0−23.7. We reduced the ESO NTT/SUSI2 archive images for this object, deriving a red-sequence redshift of $z_{\rm phot} = 0.37$. This estimate is in good agreement with the X-ray spectroscopic redshift $z_{\rm Fe} = 0.39$.
- PLCK286.3−38.4. ESO NTT/SUSI2 images and NTT/EMMI spectroscopic archive data targetting the X-ray source RX J0359.1−7205 were available. From a poor quality NTT/EMMI spectrum, we extracted a redshift of $z_{\rm spec} = 0.307 \pm 0.003$, backed-up by the presence of two absorption line features (Hβ and Mg I). Again this value agrees well with the X-ray spectroscopic redshift of $z_{\rm Fe} = 0.31$.

Finally, the source PLCK G262.7−40.9 appeared to be one of the ACT SZ optically-confirmed clusters (Menanteau et al. 2010), accepted for observation by *Chandra* after it was scheduled for observation with *XMM-Newton*. The reported photometric redshift is $z_{\rm phot} = 0.54 \pm 0.05$, in disagreement with our X-ray-derived value of $z_{\rm Fe} = 0.38$ at the 3σ level. Although slightly weak, the Fe K line is clearly seen in the X-ray spectrum (see Fig. 5 right panels). We thus adopt the X-ray estimate. However, optical spectroscopic observations are clearly needed to confirm the cluster redshift. All compiled and derived optical redshifts are reported in Col. 6 ($z_{\rm opt}$) in Table 2.

5. Physical parameter estimates of confirmed clusters

5.1. XMM-Newton data

For all single clusters (17 systems) or obvious sub-components in double and triple systems (4 objects), the X-ray peak position was taken to be the (sub-)cluster centre. For these systems we undertook a more in-depth analysis assuming that a spherically symmetric approximation is appropriate.

Surface brightness profiles, centred on the X-ray peak, were extracted in the [0.3–2] keV band in 3.″3 bins. Deprojected, PSF-corrected gas density profiles were then calculated using the method described in Croston et al. (2008). Global cluster parameters were then estimated self-consistently within R_{500} via iteration about the M_{500}–$Y_{\rm X}$ relation of Arnaud et al. (2010, see also Pratt et al. 2010), viz.,

$$E(z)^{2/5} M_{500} = 10^{14.567 \pm 0.010} \left[\frac{Y_{\rm X}}{2 \times 10^{14}\, M_\odot\, {\rm keV}} \right]^{0.561 \pm 0.018} h_{70}^{-1}\, M_\odot, \quad (1)$$

assuming the standard evolution predicted by the self-similar model purely based on gravitation. In addition, the X-ray luminosity in the [0.1–2.4] keV band interior to R_{500}, L_{500} was calculated as described in Pratt et al. (2009). All resulting X-ray properties are summarized in Table 2. Errors include only statistical uncertainties. We did not attempt to include systematic errors due to redshift uncertainty or high background level; such estimates are beyond the scope of the paper. The results for this sample are not used for quantitative statistical study (e.g. derivation of scaling laws), which would require redshift confirmation (sources with $Q_z < 2$) and deeper *XMM-Newton* observations.

The X-ray position for single systems is compared to the *Planck* position in Fig. 6. The offset behaviour is similar to that observed for known clusters in the ESZ sample (see Planck Collaboration 2011d, for discussion). Except for the outlier PLCK G18.7+23.6, the positional offset is less than 2′ and is clearly dominated by the *Planck* reconstruction error which peaks at that value. A physical offset is also expected, especially for merging clusters. Such an offset would contribute less with increasing z as it would be more and more poorly resolved. The small residual systematic variation of the offset with z, for $z > 0.2$, suggests that physical offsets may indeed slightly contribute. This is likely to be the case for PLCK G18.7+23.6, a highly disturbed object at $z = 0.09$, the lowest z of the sample, and which has an offset of 3′ corresponding to $0.3R_{500}$. In all

Table 2. X-ray and SZ properties of the confirmed *Planck* sources.

Name	S/N	RA_X	Dec_X	z_{Fe}	z_{opt}	Q_z	R	θ_{det}	R_{500}	T_X	$M_{gas,500}$	Y_X	Y_{500}	M_{500}	L_{500}
		[h:m:s]	[d:m:s]				[cts s^{-1}]	[′]	[kpc]	[keV]	[$10^{14}\,M_\odot$]	[$10^{14}\,M_\odot$ keV]	[10^{-4} Mpc^2]	[$10^{14}\,M_\odot$]	[10^{44} erg s^{-1}]
PLCK G285.0−23.7	11.5	07:23:18.4	−73:27:20.6	0.39	0.37[a]	2	1.85 ± 0.02	4.1	1216	6.98 ± 0.74	1.23 ± 0.04	8.62 ± 1.28	1.27 ± 0.35	7.71 ± 0.50	16.91 ± 0.27
PLCK G287.0+32.9	10.6	11:50:49.2	−28:04:36.5	0.39	…	1	2.68 ± 0.01	6.8	1541	12.86 ± 0.42	2.39 ± 0.03	30.69 ± 0.36	3.30 ± 0.16	15.72 ± 0.27	17.20 ± 0.11
PLCK G171.9−40.7	10.6	03:12:57.4	08:22:10.3	0.27	…	2	2.19 ± 0.03	5.3	1428	10.65 ± 0.42	1.43 ± 0.04	15.26 ± 0.72	2.05 ± 0.21	10.92 ± 0.37	11.28 ± 0.19
PLCK G271.2−31.0	8.5	05:49:19.5	−62:05:16.0	0.37	…	2	3.32 ± 0.01	5.2	1212	7.94 ± 1.23	1.02 ± 0.04	8.08 ± 1.03	1.02 ± 0.17	7.47 ± 0.70	18.95 ± 0.16
PLCK G262.7−40.9	8.3	04:38:17.2	−54:19:25.1	0.39	0.54[b]	2	1.72 ± 0.02	5.6	1169	7.77 ± 0.87	0.90 ± 0.06	7.01 ± 0.98	1.14 ± 0.22	6.87 ± 0.68	9.94 ± 0.47
PLCK G277.8−51.7	7.4	02:54:16.7	−58:56:44.0	0.44	…	1	1.33 ± 0.02	5.8	1172	6.37 ± 0.84	1.26 ± 0.02	8.01 ± 0.57	1.70 ± 0.20	7.32 ± 0.38	9.46 ± 0.07
PLCK G286.6−31.3	6.9	05:31:27.5	−75:10:41.2	0.21	…	2	1.82 ± 0.04	4.6	1149	6.85 ± 0.94	0.60 ± 0.07	4.14 ± 3.01	0.61 ± 0.32	5.32 ± 0.86	3.72 ± 0.23
PLCK G292.5+22.0	6.9	12:01:05.3	−39:52:26.2	0.30	…	2	1.42 ± 0.03	6.8	1336	9.82 ± 0.84	1.17 ± 0.04	11.49 ± 1.33	1.45 ± 0.24	9.25 ± 0.60	5.46 ± 0.09
PLCK G285.6−17.2	6.3	08:43:44.4	−71:13:13.7	0.35	…	1	0.69 ± 0.02	4.4	1044	4.87 ± 0.35	0.71 ± 0.01	3.46 ± 0.40	0.79 ± 0.13	4.67 ± 0.22	4.45 ± 0.08
PLCK G18.7+23.6	6.0[c]	17:02:21.3	−00:59:58.9	0.09	…	2	3.94 ± 0.01	10.5	1034	4.63 ± 0.32	0.39 ± 0.02	1.80 ± 0.32	0.32 ± 0.17	3.42 ± 0.22	1.21 ± 0.05
PLCK G4.5−19.5	5.9	19:17:04.6	−33:31:21.9	0.54	…	2	1.29 ± 0.02	4.8	1245	10.39 ± 0.52	1.37 ± 0.03	14.27 ± 0.87	1.99 ± 0.20	9.88 ± 0.35	17.78 ± 0.11
PLCK G241.2−28.7	5.7	05:42:56.8	−35:59:54.8	0.42	…	2	0.92 ± 0.02	3.6	1065	6.08 ± 0.32	0.75 ± 0.02	4.58 ± 0.39	0.79 ± 0.11	5.37 ± 0.20	6.72 ± 0.12
PLCK G272.9+48.8	5.4	11:33:10.5	−09:28:52.2	0.40	…	2	0.66 ± 0.01	3.7	1053	4.67 ± 0.32	0.88 ± 0.02	4.09 ± 0.32	0.87 ± 0.18	5.07 ± 0.21	12.36 ± 0.09
PLCK G205.0−63.0	5.3	02:46:25.8	−20:33:16.9	0.31	…	2	1.12 ± 0.03	5.5	1111	6.06 ± 0.39	0.72 ± 0.02	4.38 ± 0.30	0.83 ± 0.09	5.37 ± 0.21	3.89 ± 0.08
PLCK G250.0+24.1	5.2	09:32:13.8	−17:38:06.7	0.40	…	0	0.18 ± 0.02	3.8	1061	6.75 ± 0.28	0.63 ± 0.03	4.27 ± 0.42	0.72 ± 0.12	5.19 ± 0.21	3.37 ± 0.19
PLCK G286.3−38.4	5.1	03:59:10.2	−72:04:46.1	0.31	0.307 ± 0.003[d]	2	0.32 ± 0.05	4.5	1064	5.60 ± 0.14	0.62 ± 0.01	3.48 ± 0.08	0.80 ± 0.06	4.72 ± 0.08	4.07 ± 0.02
PLCK G100.2−30.4	4.7	23:22:14.9	28:31:13.5	0.31	0.38 ± 0.04[a]	0	0.76 ± 0.01	4.7	1128	9.03 ± 0.30	0.53 ± 0.02	4.76 ± 0.29	0.45 ± 0.14	5.63 ± 0.22	3.36 ± 0.08
PLCKG308.3−20.2	8.3														
A	…	15:18:55.5	−81:30:30.1	0.48	…	2	1.06 ± 0.01	3.9	1250	9.55 ± 0.56	1.31 ± 0.04	12.55 ± 0.92	…	9.32 ± 0.38	15.65 ± 0.19
B	…	15:16:52.6	−81:35:50.0	0.48[f]	…	−1	0.42 ± 0.01	2.9	894	3.79 ± 0.35	0.55 ± 0.03	2.09 ± 0.25	…	3.41 ± 0.23	8.67 ± 0.26
PLCKG337.1−26.0	6.6														
A	…	19:14:37.7	−59:28:16.7	0.26	…	2	3.28 ± 0.03	7.5	1177	6.16 ± 0.23	0.86 ± 0.01	5.30 ± 0.25	…	6.05 ± 0.16	8.95 ± 0.07
b	…	19:13:51.4	−59:33:51.6	0.12	…	2	1.79 ± 0.02	4.5	749	2.84 ± 0.20	0.12 ± 0.01	0.34 ± 0.03	…	1.34 ± 0.07	1.02 ± 0.01
PLCKG214.6+36.9	3.6														
A	…	09:08:49.5	14:38:29.4	0.45	0.45[d]	2	0.38 ± 0.01	4.3	767	3.46 ± 0.26	0.25 ± 0.01	0.85 ± 0.09	…	2.08 ± 0.12	3.03 ± 0.07
B	…	09:09:02.1	14:39:41.7	0.45	0.46[a]	1	0.11 ± 0.01	2.3	750	4.16 ± 0.75	0.18 ± 0.01	0.76 ± 0.18	…	1.94 ± 0.26	1.03 ± 0.06
C	…	09:08:51.4	14:45:55.3	0.45[f]	0.45[d]	−1	0.25 ± 0.01	3.1	809	3.72 ± 0.50	0.30 ± 0.01	1.13 ± 0.19	…	2.44 ± 0.23	2.28 ± 0.08
PLCKG334.8−38.0	3.4														
A	…	20:52:16.8	−61:12:29.4	0.35[e]	…	2	0.13 ± 0.01	1.8	722	3.14 ± 0.33	0.15 ± 0.01	0.48 ± 0.07	…	1.55 ± 0.13	0.77 ± 0.06
B	…	20:53:08.0	−61:10:35.3	0.35[f]	…	−1	0.08 ± 0.01	3.2	605	2.02 ± 0.31	0.09 ± 0.01	0.19 ± 0.05	…	0.91 ± 0.12	0.47 ± 0.33
C	…	20:52:44.3	−61:17:24.5	0.35[f]	…	−1	0.03 ± 0.00	1.2	607	3.13 ± 1.71	0.06 ± 0.02	0.19 ± 0.18	…	0.92 ± 0.44	0.21 ± 0.06

Notes. Column (2): signal-to-noise ratio derived from the 10-month *Planck* maps on the basis of which the ESZ sample was constructed. Columns (3)–(8): right ascension and declination of the peak of the X-ray image (J2000). Column (9): redshift from X-ray spectral fitting. Column (10): optical redshift. Column (11): Quality flag for the X-ray redshift measurement (see Sect. 4.1). Column (12): total EPIC count rates in the [0.3−2] keV band, within the maximum radius of detection given in Col. (13). Columns (14)–(20): R_{500} is the radius corresponding to a density contrast of 500, estimated iteratively from the M_{500}–Y_X relation (Eq. (1)), where $Y_X = M_{g,500}T_X$ is the product of the gas mass within R_{500} and the spectroscopic temperature T_X, and M_{500} is the total mass within R_{500}. L_{500} is the luminosity in the [0.1−2.4] keV band and in the R_{500} aperture. Y_{500} is the spherically integrated Compton parameter measured with *Planck*, centred on the X-ray peak, interior to R_{500} as estimated with *XMM-Newton*. [(a)] Photometric redshift. See Appendix A.1. [(b)] Photometric redshift for ACT-CL J0438-5419 in Menanteau et al. (2010). [(c)] Rounded from 5.99 to 6.0, therefore not included in ESZ (Planck Collaboration 2011d). [(d)] Spectroscopic redshift. [(e)] Redshift constrained from Fe L complex. [(f)] Redshift assumed to be identical to that of component *A*.

cases, the offset remains smaller than θ_{500} or the cluster extent (see also Fig. 3).

5.2. *Planck* refined Y_{SZ} estimate

The SZ signal extraction procedure is described in detail in Planck Collaboration (2011d). It consists of applying multi-frequency matched filters to the data that maximally enhance the signal-to-noise ratio of an SZ cluster source by optimally filtering the data. As shown in Planck Collaboration (2011d), SZ fluxes derived using this method can be significantly overestimated due to an over-estimation of the cluster size θ_{500}.

We can optimise the SZ photometry of the clusters presented here by using the X-ray estimate of the cluster position and size θ_{500}, derived from R_{500} measured using the M_{500}–Y_X relation as detailed in Sect. 5.1. For each cluster in the sample, we thus re-extract the SZ flux, calculating Y_{500} with the X-ray position and size fixed to the refined values derived from the high-quality *XMM-Newton* observation. The resulting Y_{500} values are listed in Table 2. In Fig. 7, they are compared to the blind values as a function of the ratio of the *XMM-Newton* and blind characteristic size θ_{500}. For most cases the values are consistent within the errors; however, there is a clear trend of SZ flux overestimation with size overestimation, which can reach as much as a factor of two (see detailed discussion of the cluster size-flux relation in Planck Collaboration 2011d and Planck Collaboration 2011g).

6. X-ray and SZ properties of newly detected clusters

In this Section we consider the 17 systems confirmed as single-component clusters of galaxies, leaving aside the multiple systems which are discussed in the next section.

6.1. RASS *properties*

We extracted $2^\circ \times 2^\circ$ count images in the [0.5–2.] keV hard band from the RASS data at the position of each cluster. We excised events associated with known RASS-BSC and RASS-FSC sources (Voges et al. 1999, 2000). We then carefully followed the methods described in Böhringer et al. (2000) and Reiprich & Böhringer (2002) to compute background corrected growth curves and estimate an associated detection radius, R_d. The background was estimated from an outer annulus with $15' < \theta < 90'$. When allowed by the quality of the growth curve, the count rate within the R_{500} aperture was either taken as the count rate within R_d when $R_d < R_{500}$ or interpolated on the curve when $R_d > R_{500}$. In the case of low quality growth curves, we computed a direct integrated count rate from the map within an aperture of R_{500}. Assuming the best fitting *XMM-Newton* spectral parameters for each cluster (i.e. z, temperature, abundance, galactic N_H) we derived the [0.1–2.4] keV band RASS flux.

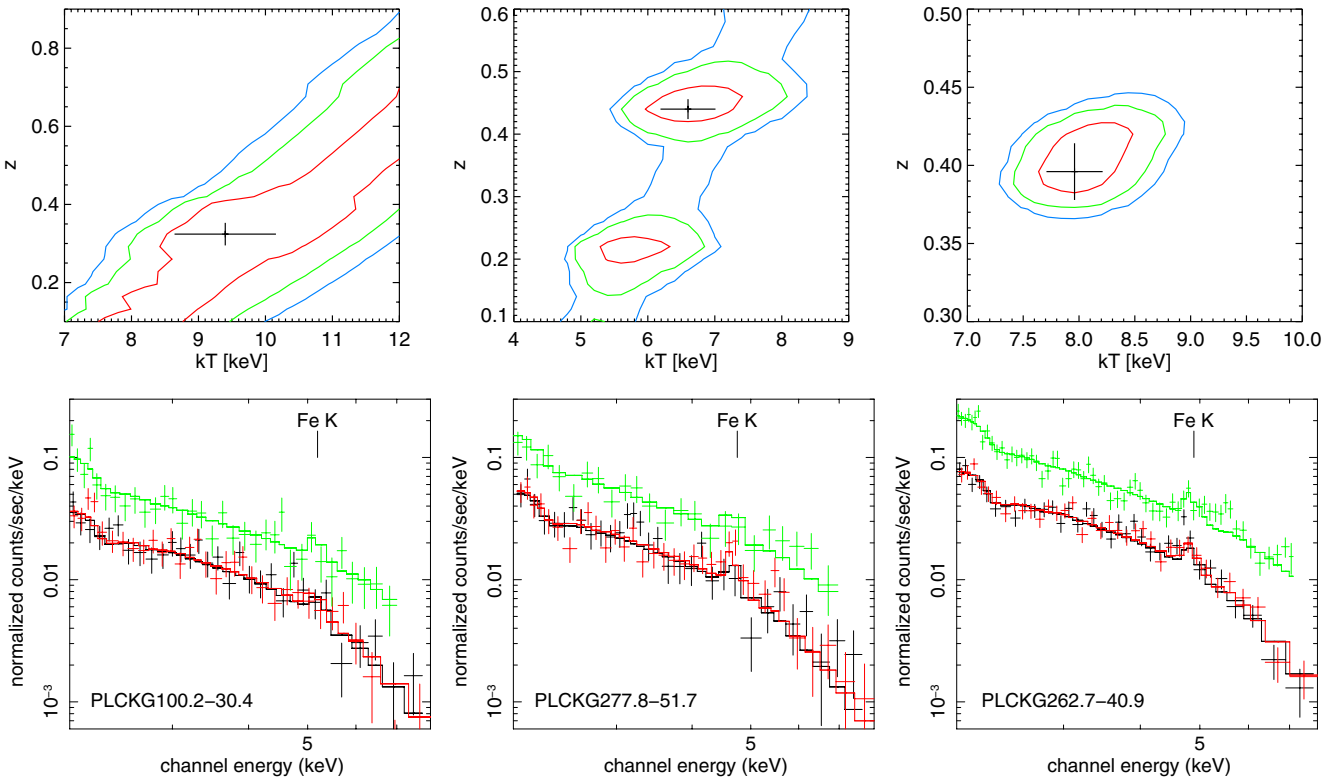

Fig. 5. *Top row*: redshift determination from *XMM-Newton* spectroscopy in the kT-z plane. Red, green and blue contours trace 68, 95 and 99.9 percent confidence levels, respectively. The black error point shows the final best-fitting spectral results with associated statistical errors. *Bottom row*: EPIC EMOS1&2 (red and black points) and EPN (green points) spectra. Only the data points above 2 keV are shown for clarity but data down to 0.3 keV are used in the spectral fitting. The line is the thermal model for the best-fitting redshift. The position of the redshifted Fe K line is marked. *From left to right* the figures are for sources PLCK G100.2−30.4, PLCK G277.8−51.7 and PLCK G241.2−28.7.

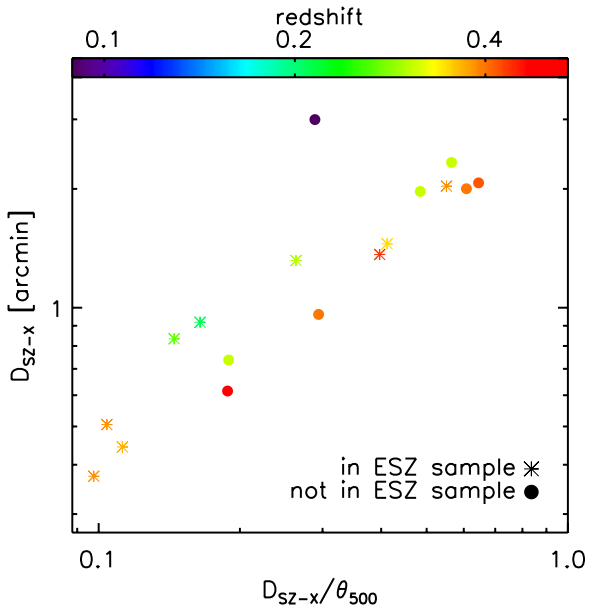

Fig. 6. Distance of blind SZ position to X-ray position, D_{SZ-X}, as a function of D_{SZ-X}, normalised to the cluster size $\theta_{500,X}$ for single confirmed systems. The clusters are colour-coded according to redshift. Note that the offset is typically less than 2′ and always less than θ_{500}.

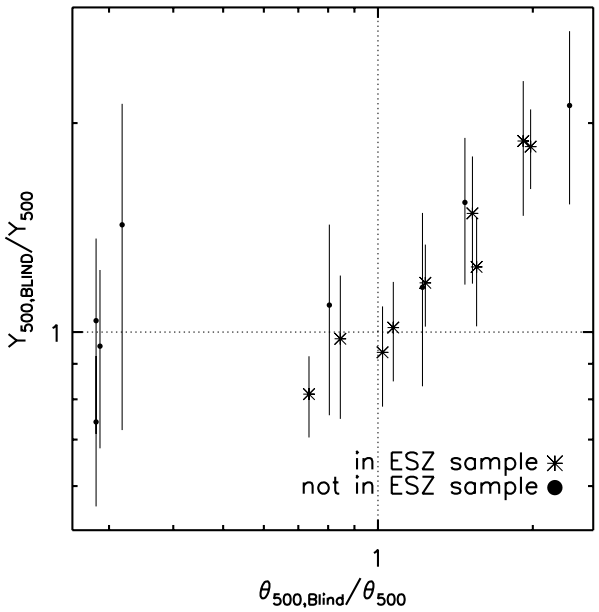

Fig. 7. Comparison of the *Planck* blind and X-ray constrained Y_{500} measurements for single confirmed systems (see text, Sect. 5.2). The ratio is correlated with the ratio of the corresponding characteristic size, θ_{500}.

The RASS values are compared to the *XMM-Newton* values in Fig. 8. There is a good agreement after taking into account the RASS statistical errors. The slight offset (<20%) is likely due to systematic errors linked to the RASS background estimate and/or calibration uncertainties. The most significant outlier at high flux is PLCK G18.7+23.6. A bright point source is present at the centre of this object (see Fig. 3) that cannot be excised from the RASS data and which contaminates the signal. From the *XMM-Newton* image (Fig. 3), the known

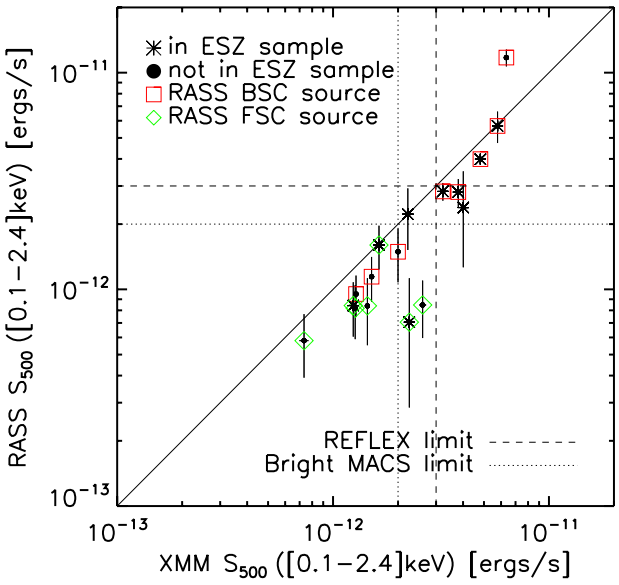

Fig. 8. Unabsorbed RASS flux versus *XMM-Newton* flux for the 17 confirmed single-component clusters. The [0.1–2.4] keV flux is measured within an aperture of θ_{500}. Clusters coincident with a RASS-BSC or a RASS-FSC source are marked with red squares and green diamonds, respectively. The most significant outlier at high flux is PLCK G18.7+23.6 at $z = 0.09$ (see Sects. 6.1 and 6.2 for discussion).

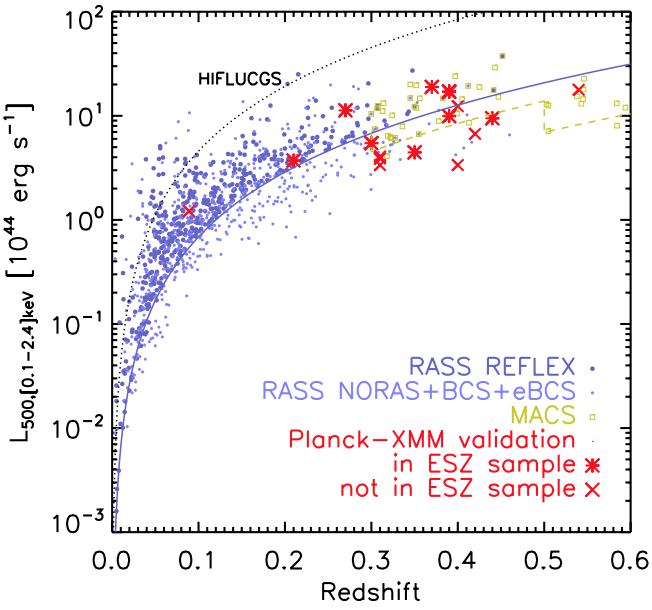

Fig. 9. The new SZ-discovered *Planck* clusters compared to clusters from the ROSAT All-Sky Survey catalogues in the L_X–z plane. The X-ray luminosity is that in the [0.1–2.4] keV band. Catalogues shown are the REFLEX, NORAS, BCS, eBCS and published MACS catalogues. The solid line is the REFLEX flux limit of 3×10^{-12} erg s^{-1} cm^{-2}, similar to that of the BCS+eBCS catalogues. The dotted line is the HIFLUCGS flux limit of 2×10^{-11} erg s^{-1} cm^{-2} and the dashed line is from the MACS flux limits. See Sect. 6.2 for references and details.

RASS-FSC or RASS-BSC sources within the *Planck* error box for 15 of the candidates can be clearly identified with the clusters. Those are indicated in Fig. 8. The two clusters with no RASS-FSC or RASS-BSC association, PLCK G287.0+32.9 and PLCK G292.5+22.0, are in fact detected in RASS, but at low S/N (2 and 3, respectively; see also Sect. 6.4).

6.2. The L_{X-z} plane and comparison with RASS catalogues

In Fig. 9, the new clusters are shown in the L_X–z plane, plotted together with the clusters from large catalogues based on RASS data outside the Galactic Plane: REFLEX (Böhringer et al. 2004) in the Southern sky: NORAS (Böhringer et al. 2000); BCS (Ebeling et al. 1998); and eBCS (Ebeling et al. 2000) in the Northern Sky. The NORAS is not flux limited. The REFLEX flux limit of 3×10^{-12} erg s^{-1} cm^{-2} is shown. It is similar to that of the eBCS+BCS limit of 2.8×10^{-12} erg s^{-1} cm^{-2}. Also shown are clusters from the published catalogues of the MACS survey with their corresponding flux limit. MACS is based on the RASS-BSC but in contrast to the above surveys, the X-ray extent of the RASS source is not a selection criterion, allowing more distant (but massive) clusters to be found (Ebeling et al. 2001). Published MACS catalogues are the $z > 0.5$ catalogue (Ebeling et al. 2007) and the $0.3 < z < 0.5$ brightest cluster catalogue (Ebeling et al. 2007, hereafter bright MACS). Luminosities plotted in Fig. 9 are the homogenised values given in the MCXC (Meta-Catalogue of X-ray detected Clusters of galaxies Piffaretti et al. 2011).

The present sample of new *Planck*-detected systems spans a redshift range of $0.1 \lesssim z \lesssim 0.6$, with 15 out of 17 clusters above $z = 0.25$, a medium-distant redshift region of the L_X–z plane that is sparsely-populated by the RASS catalogues. As a consequence, our current sample has X-ray luminosities well below the flux limit of HIFLUCGS (Reiprich & Böhringer 2002) and REFLEX-DXL (Zhang et al. 2006), two high-luminosity X-ray selected samples that stand as the counterparts to our present high S/N SZ sample. The closest sample in X-ray luminosity and redshift to the new *Planck* clusters are the MACS clusters, although the *Planck* clusters go to lower luminosity.

Most of the new *Planck* clusters naturally fall below the REFLEX flux limit or, equivalently, the BCS+eBCS limit in the North. However, three clusters lie well above this limit: PLCK G18.7+23.6, PLCK G171.9−40.7, PLCK G271.2−31.0, in order of decreasing X-ray flux (Figs. 8 and 9). As discussed above, PLCK G18.7+23.6 at $z = 0.09$ has a very bright central source and very diffuse ICM emission. It may have been misclassified as a point source in the REFLEX survey. We also note that this cluster, although not included in the ESZ sample, is the brightest X-ray cluster of the sample due to its low redshift $z = 0.09$. PLCK G271.2−31.0 simply falls in the Large Magellanic Cloud LMC2 region, which was excluded in the REFLEX survey (see Böhringer et al. 2001, Table 1). However, PLCK G171.9−40.7 at $z = 0.27$ has a flux of 5.7×10^{-12} erg s^{-1} cm^{-2} (from fully consistent ROSAT and *XMM-Newton* measurements), and is a northern sky cluster that fulfills the BCS flux and sky position criteria. Thus a priori, it should have been included in that survey. Finally, six new clusters at $z \geq 0.3$ are above the MACS flux limit. Of these, four are not associated with a RASS-BSC source and so could not be found in a MACS-like survey, and the other two are at lower declination than considered by MACS.

6.3. Gas morphology and scaled density profiles

Figure 3 shows [0.3–2] keV *XMM-Newton* images of the newly-discovered clusters. Each image corresponds to the same physical size in units of R_{500} and is corrected for surface brightness dimming with redshift and divided by the emissivity in the [0.3–2] keV energy band. As detailed in Arnaud et al. (2002, Sect. 3.2), the emissivity is computed from a redshifted thermal model convolved with the instrument response and taking into account Galactic absorption. The resulting image is proportional

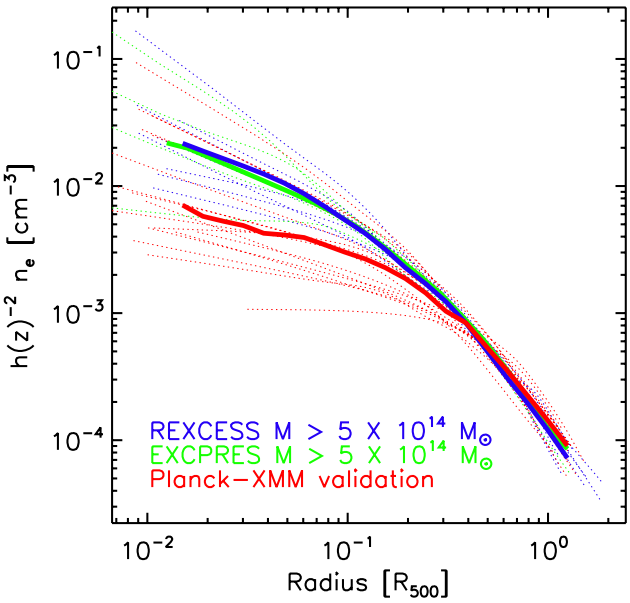

Fig. 10. Scaled density profiles of the new *Planck* SZ clusters compared to those of similar mass systems from the representative X-ray samples REXCESS (Böhringer et al. 2007) and EXCPRES (Arnaud et al., in prep.). R_{500} is estimated from the M_{500}–Y_X relation of Arnaud et al. (2010). Thick lines show the mean profile of each sample. The density profiles of the *Planck* SZ-selected clusters are on average shallower than those of the X-ray selected clusters of the same mass.

to the emission measure along the line of sight, which is then scaled by $E(z)^2 R_{500}$ according to the self-similar model. The colour table is the same for all clusters, so that the images would be identical if clusters obeyed strict self-similarity. A first visual impression is that low surface brightness, morphologically-disturbed objects dominate the sample, which contains very few centrally-peaked, cool core-like objects.

The visual impression is confirmed and quantified when one looks at the density profiles of the clusters shown in Fig. 10. They are plotted together with the density profiles of similar mass clusters from the representative X-ray-selected samples REXCESS ($z < 0.2$; Böhringer et al. 2007) and EXCPRES ($0.4 < z < 0.6$; Arnaud et al, in prep.). For all three samples, the radii are scaled by R_{500}, estimated from the M_{500}–Y_X relation (Eq. (1)). The thick lines show the mean profile. While the two X-ray-selected samples agree to a remarkable degree, the *Planck*-selected sample clearly consists of systems with much flatter density profiles, and the corresponding mean profile is significantly flatter than that of the X-ray selected samples. This shape is due to a number of very disturbed clusters with very flat profiles in the new *Planck*-discovered cluster sample. Let us consider the ten clusters with the flattest density profiles, flatter than the mean profile *Planck* cluster profile and flatter than all the REXCESS profiles. These ten objects include PLCK G18.7+23.6 at $z = 0.09$ discussed above, PLCK G286.6−31.3 at $z = 0.21$ that is just at the REFLEX flux limit and PLCK G292.5+22.0 at $z = 0.30$ that is just at the MACS flux limit (Fig. 9). The other seven clusters lie at medium redshift, $0.3 < z < 0.45$, and are all hot ($T_X \gtrsim 5$ keV) and massive ($M_{500} \gtrsim 5 \times 10^{14}\, M_\odot$) systems. They lie below the flux limit of both REFLEX and bright MACS for a similar mass range (Ebeling et al. 2010). Thus *Planck* appears to have uncovered a population of massive, disturbed, low-luminosity systems.

6.4. SZ flux versus X-ray prediction and mass-proxy – mass relations

Planck Collaboration (2011g) uses *XMM-Newton* archival data to study the relations between the SZ signal and X-ray properties such as Y_X or the soft band luminosity L_{500} on a sub-sample of clusters from the high signal-to-noise ratio ESZ sample. This sample (hereafter the ESZ-*XMM*-archive sample) is SZ selected but by nature only comprises clusters from X-ray surveys. As discussed extensively in Planck Collaboration (2011g), the analysis has demonstrated the excellent agreement between the observed scaling relations and the predictions based on REXCESS pressure profiles and numerical simulations (Arnaud et al. 2010). In Fig. 11, we have placed the new *Planck XMM-Newton* confirmed clusters on the Y_{500}–Y_X relations (top panels) and the L_{500}–Y_{500} and M_{500}–L_{500} relations (bottom panels).

6.4.1. The Y_{500}–Y_X relation

The SZ signal, Y_{500}, is plotted as a function of the normalized $D_A^{-2} Y_X$ parameter in the left panel of Fig. 11. The new clusters follow the trend observed for the ESZ-*XMM*-archive and are consistent with the REXCESS prediction (blue line). However, a slight turnover is observed at low flux, with observed points systematically above the predicted relation. This excess is likely due to the Malmquist bias. Such a trend is also slightly apparent for the ESZ-*XMM*-archive sample but is less important (see Planck Collaboration 2011g, for discussion of this effect). The low flux clusters span various z values and are redistributed over the range of intrinsic Compton parameter. As a result there is slight positive offset apparent in the $D_A^2 Y_{500}$–Y_X relation for new clusters as compared to the ESZ-*XMM*-archive sample.

This suggests that as far as the relation between Y_{500} and its X-ray equivalent Y_X is concerned, the new clusters are similar to X-ray selected clusters, although they are more dynamically disturbed. This is expected if indeed the pressure is the quantity less affected by dynamical state and both Y_X and Y_{500} are low scatter mass proxies. However, independent mass estimates are required to check this point; they cannot be provided by X-ray measurements in view of the highly unrelaxed nature of the new clusters.

6.4.2. The L_{500}–Y_{500} and M_{500}–L_{500} relations

As compared to X-ray selected clusters, the new clusters fall on the low luminosity side of the L_{500}–Y_{500} relation (bottom left panel of Fig. 11). In other words, they are under-luminous at given Y_{500}. If the mass is indeed tightly related to Y_{500} (or Y_X) we then expect them to be underluminous at a given mass. This trend is consistently observed in the bottom-right panel, where M_{500} is estimated from Y_X: the new clusters fall towards the high-mass, low-luminosity side of the M_{500}–L_{500} relation. However, confirmation requires independent mass estimates, e.g., from lensing data.

As shown by Pratt et al. (2009), the underluminous region of the L–M plane is populated by morphologically disturbed systems. This once again suggests that the majority of the new *Planck*-detected systems are disturbed, in agreement with the above discussion on the morphology and the scaled density profiles.

The dispersion of the new clusters about the M_{500}–L_{500} relation also seems higher than that for X-ray selected objects. This suggests the existence of new extreme low-luminosity, high-mass objects that are being revealed by *Planck*. The two prominent outliers are PLCK G287.0+32.9 ($z = 0.39$) and

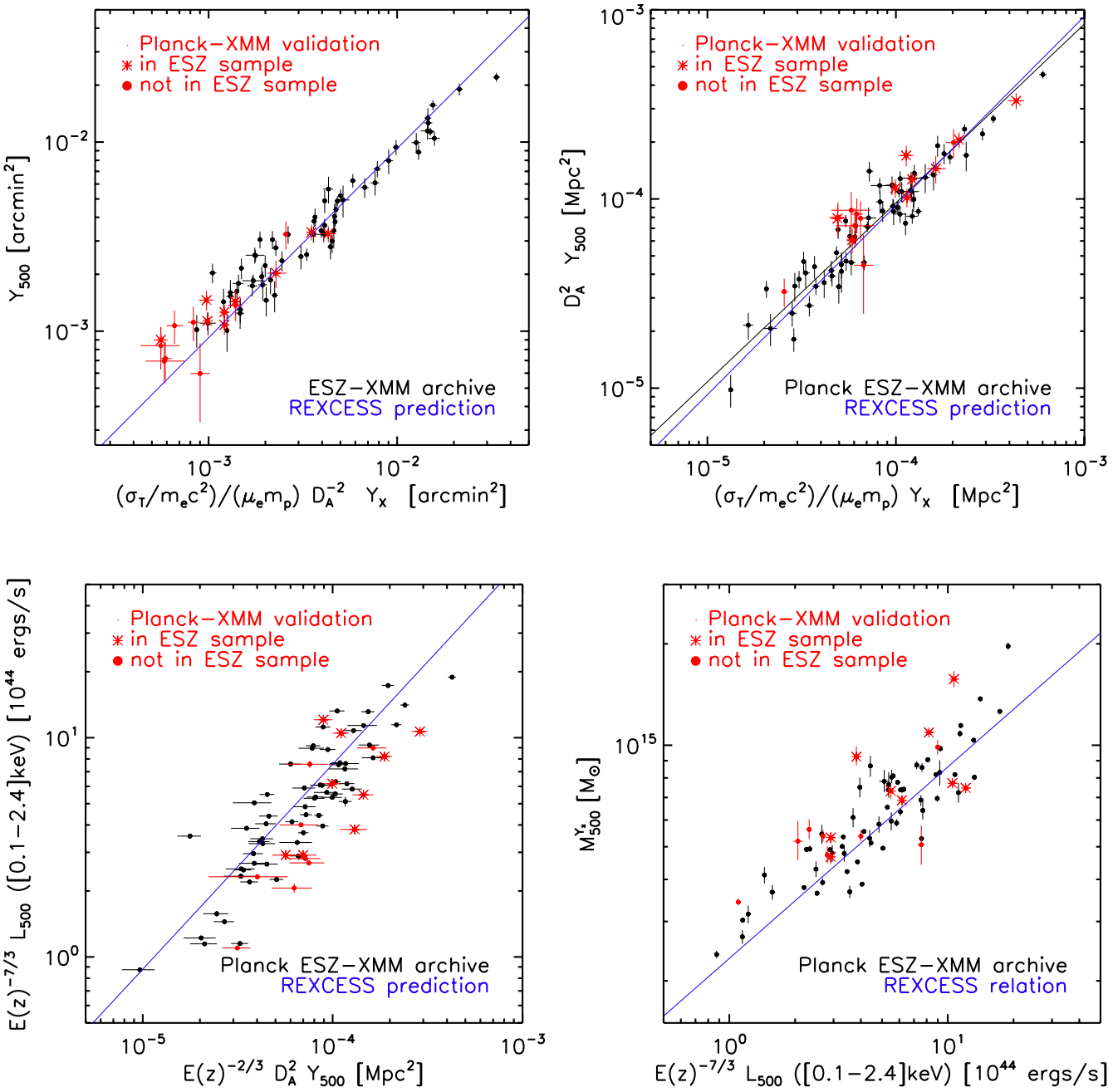

Fig. 11. Scaling relations for the 17 new confirmed single-component clusters (red symbols). Black points show clusters in the *Planck*-ESZ sample with *XMM-Newton* archival data as presented in Planck Collaboration (2011g). The solid black line denotes the corresponding scaling relation fits in each panel. The blue lines in *the top and bottom right panels* denote the predicted Y_{500} scaling relations from the REXCESS X-ray observations (Arnaud et al. 2010). The blue line in *the bottom left panel* is the Malmquist bias corrected M–L relation from the REXCESS sample (Pratt et al. 2009; Arnaud et al. 2010). In *all figures*, R_{500} and M_{500} are estimated from the M_{500}–Y_X relation of Arnaud et al. (2010). *Top row*: relation between apparent SZ signal (Y_{500}, *left*) or intrinsic Compton parameter ($D_A^2 Y_{500}$, *right*) and the corresponding normalised Y_X parameter. *Bottom row*: relation between X-ray luminosity and Y_{500} (*left*) and between mass and luminosity (*right panel*). The new clusters are on average less luminous at a given Y_{500}, or more massive at a given luminosity, than X-ray selected clusters.

PLCK G292.5+22.0 ($z = 0.3$), detected by *Planck* at high S/N values of 10.6 and 6.9, respectively. They belong to the very hot ($T \gtrsim 10$ keV) and very massive ($M_{500} \gtrsim 10^{15}\,M_\odot$) cluster category (Table 2) and are the only two clusters associated with neither a BSC nor an FSC source (Sect. 6.1 and Fig. 8). The flux of PLCK G292.5+22.0 barely reaches the MACS limit for a mass of $M_{500} \sim 9.2 \times 10^{14}\,M_\odot$. It has a very disturbed morphology (Fig. 3) and a flat density profile with a scaled central density of 4×10^{-3} cm^{-3} (Fig. 10).

7. Further analysis of multiple systems

7.1. Double systems

Two of the new *Planck* sources (PLCK G308.3−20.2 and PLCK G337.1−26.0) were revealed by the *XMM-Newton* validation observations to be double systems. X-ray images of these systems are included in the gallery in Fig. 3.

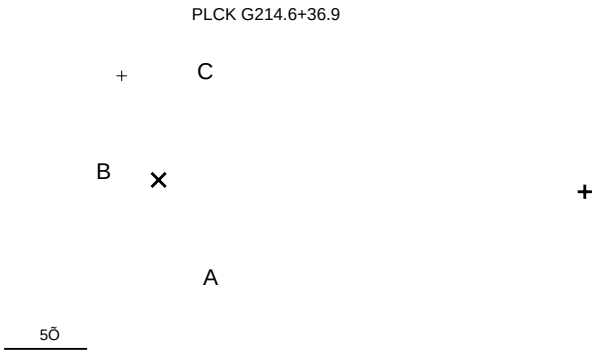
PLCK G214.6+36.9
C
B
A
5Õ

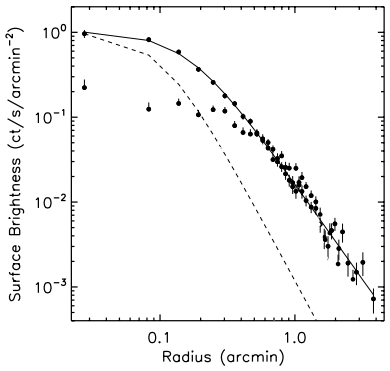
Surface Brightness (ct/s/arcmin^{-2})
10^{0}
10^{-1}
10^{-2}
10^{-3}
0.1
1.0
Radius (arcmin)